

1 **An experiment to test satellite radar interferometry-observed geodetic ties**  
2 **to remotely monitor vertical land motion at tide gauges**

3

4 M.S. Filmer<sup>1</sup>, S.P.D. Williams<sup>2</sup>, C.W. Hughes<sup>2,3</sup>, G. Wöppelmann<sup>4</sup>,

5 W.E. Featherstone<sup>1</sup>, P.L. Woodworth<sup>2</sup>, A.L. Parker<sup>1,5</sup>

6

7 1. School of Earth and Planetary Sciences, Curtin University, GPO Box U1987, Perth, WA 6845, Australia

8 2. National Oceanography Centre, Joseph Proudman Building, 6 Brownlow Street, Liverpool, L3 5DA, UK

9 3. School of Environmental Sciences, University of Liverpool, Liverpool, L69 3GP, UK

10 4. Littoral, Environment and Societies (LIENS), University of La Rochelle – National Centre for Scientific  
11 Research (CNRS), 2 rue Olympe de Gouges, 17000 La Rochelle, France

12 5. Centre for Earth Observation, CSIRO Astronomy and Space Science, 26 Dick Perry Avenue, Kensington,  
13 WA 6155, Australia

14 Corresponding author: [M.Filmer@curtin.edu.au](mailto:M.Filmer@curtin.edu.au)

15

16 ORCIDs

17 M.S. Filmer: <http://orcid.org/0000-0002-3555-4869>

18 S.P.D. Williams: <http://orcid.org/0000-0003-4123-4973>

19 C.W. Hughes: <http://orcid.org/0000-0002-9355-0233>

20 G. Wöppelmann: <http://orcid.org/0000-0001-7178-2503>

21 W.E. Featherstone: <http://orcid.org/0000-0001-9644-4535>

22 P.L. Woodworth: <http://orcid.org/0000-0002-6681-239X>

23 A.L. Parker: <http://orcid.org/0000-0003-4342-9301>

24

25

26

27

28 **Abstract:** The nature and linearity of vertical land motion (VLM) impacting the global sea  
29 level record from tide gauges is not well known, but remains of importance to understand  
30 long-term changes to sea level. Local surveys are required to directly measure VLM at tide  
31 gauges relative to a global reference frame, but this is limited by the lack of differential VLM  
32 measurements between tide gauges and continuously operating GPS (cGPS) stations that are  
33 not co-located, i.e., fixed to the tide gauge structure. We present results from an experiment  
34 using satellite radar interferometry (InSAR) scenes acquired from the TerraSAR-X satellite  
35 mission to test whether InSAR could replace repeat geodetic levelling as a ‘geodetic tie’  
36 between cGPS stations and tide gauges. Comparisons are made among TerraSAR-X (TSX),  
37 cGPS and tide gauge minus altimetry VLM estimates for the Hillarys and Fremantle tide  
38 gauges (Perth, Western Australia), which are used as test sites for this method. The results  
39 suggest agreement between differential TSX and altimetry minus tide gauge VLM rates, but  
40 systematic offsets among the absolute/geocentric rates where the TSX is referenced to IGS08  
41 at the PERT cGPS. The TerraSAR-X VLM at the Fremantle tide gauge for the period 7  
42 October 2012 – 7 October 2017 is  $+0.45 \pm 0.40$  mm/yr (referenced to IGS08 at PERT cGPS),  
43 although this should be treated cautiously over this short period, and also that VLM at  
44 Fremantle and Hillarys appear to be non-linear over time. We infer from this that the  
45 uncertainties in TerraSAR-X differential VLM rates are comparable to those from the highest  
46 quality repeat levelling, although the uncertainty approaches  $\pm 1$  mm/yr if the reference point  
47 uncertainty of the TSX and cGPS are considered when transformed to a terrestrial reference  
48 frame.

49  
50 **Key words:** InSAR, sea level change, vertical land motion, tide gauges

51  
52  
53  
54  
55  
56

**57 1. Introduction**

58 Estimates of sea level change (SLC) rates and their de/acceleration determined by tide gauges  
59 fixed to the Earth's surface are susceptible to vertical land motion (VLM), i.e., subsidence or  
60 uplift, at their locations. Studies have focussed on these effects on global (e.g., Wöppelmann  
61 and Marcos 2016; Hamlington et al. 2016; Santamaría-Gómez et al. 2017) and local (e.g.,  
62 Raucoules et al. 2013; Wöppelmann et al. 2013; Featherstone et al. 2015; Bekaert et al. 2017;  
63 Poitevin et al. 2019) scales. Tide gauges undergoing subsidence will imply an inflated rate of  
64 sea level rise, and those experiencing uplift will show a lower rate of sea level rise, and  
65 potentially sea level fall if the uplift is larger than the magnitude of long-term sea level rise,  
66 such as in Fennoscandia and northern North America (e.g., Mazzotti et al. 2008). An  
67 additional complexity is that non-linear VLM may imply artificial acceleration or  
68 deceleration, or simply mask any real change in the linear rate of SLC.

69       Tide gauge VLM can be caused by anthropogenic effects due to  
70 groundwater/fluid/gas extraction (e.g., Fielding et al. 1998; Brooks et al. 2007; Raucoules et  
71 al. 2013) or natural variation at regional scale due to tectonics, glacial isostatic adjustment  
72 (GIA), or a combination of some or all (e.g., Wöppelmann and Marcos 2016). Various  
73 methods have been used to estimate tide gauge VLM, including the use of continuous GPS  
74 (cGPS) stations at or near tide gauges (Bevis et al. 2002), GIA models (Peltier 2004), and  
75 subtraction of satellite altimetry measurements of the sea surface adjacent to the tide gauge  
76 from the sea level recorded by the tide gauge (Kuo et al. 2004). In the latter, the difference is  
77 taken to be VLM at the tide gauge, on the assumption that the altimetry and tide gauge sea  
78 level records should be observing the same sea level rate in the absence of any artefacts  
79 (Wöppelmann and Marcos, 2016).

80       While all of these methods provide estimates of tide gauge VLM, they have  
81 limitations, either in their measurement and processing, or that they may not be directly

82 measuring VLM at the tide gauge. For example, cGPS may be placed near tide gauges, but  
83 still a kilometre or more away (e.g., King et al. 2012), so that local differential VLM between  
84 the cGPS station and the tide gauge will mean that the VLM rate from the cGPS time series  
85 may be different to the actual rate at the tide gauge (e.g., Featherstone et al. 2015). The  
86 conventional method of monitoring differential VLM between the tide gauge and a cGPS  
87 station is by repeat differential levelling, which as a quality control for first order standard  
88 surveys usually has a maximum allowable misclosure of  $2\sqrt{d}$  mm ( $d$  is the one way distance  
89 between levelling endpoints in km) for two-way levelling forward and reverse between  
90 benchmarks. Note, though, that levelling measures differential VLM relative to a geopotential  
91 surface. When the geopotential is also changing, this can differ from the purely geometric  
92 definitions of VLM from other techniques. In general, it is expected that these differences  
93 will be negligible over a few kms compared to the differential VLM itself.

94 An example of the precision of high quality levelling is Lyon et al. (2018), who used  
95 an east-west repeat levelling traverse across the Perth Basin to demonstrate that when best  
96 practice in field and processing procedures are followed, a misclosure precision of  $\sim 0.45\sqrt{d}$   
97 mm can be achieved. This standard of levelling was shown to achieve rate uncertainties of  
98 between  $\pm 0.10$  mm/yr and  $\pm 1.87$  mm/yr over four years for a 65-benchmark  $\sim 40$  km long  
99 repeat levelling line. The median for these uncertainties is  $\pm 0.44$  mm/yr, which could be  
100 considered a best case precision over a  $\sim 4$  year levelling time series, with two repeat surveys  
101 conducted each year. Woodworth et al. (2017) refer to a repeat levelling connection between  
102 a tide gauge and a cGPS station as a 'geodetic tie', however, this connection is often not done  
103 by the agencies usually tasked with the surveys, usually due to funding/resource constraints  
104 and the perceived low priority placed on these ties.

105 A feasible alternative to determine differential VLM between tide gauges and cGPS  
106 stations is shown here through the use of satellite-borne InSAR (interferometric synthetic

107 aperture radar), and more specifically, methods such as persistent scatterer interferometry  
108 (PSI) (e.g., Feretti et al. 2000; Kampes 2006; Hooper et al. 2007), and/or small baseline  
109 multi-temporal InSAR (MTI; Hooper 2008; Hooper et al 2012). InSAR has been  
110 demonstrated to estimate line of sight (LoS to satellite) land displacement at 1 mm/yr  
111 precision, or in some circumstances less, depending on the number of SAR scenes and length  
112 of the time series (e.g., Rucci et al. 2012; Cao et al. 2018). There have been a number of  
113 InSAR studies that have investigated coastal VLM, including near tide gauges, e.g., Brooks et  
114 al. (2007) in the Los Angeles area, Adamska (2012) at tide gauges in the UK, Raucoules et al.  
115 (2013) in Manila, the Philippines, Wöppelmann et al. (2013) in Alexandria, Egypt, Le  
116 Cozannet et al. (2014; 2015) in Dakar, Senegal, Bekaert et al. (2017) in the Chesapeake Bay  
117 region of the USA, and Poitevin et al. (2019) at Brest, France. All of these have used InSAR  
118 to estimate VLM in the coastal area surrounding the tide gauge(s), inferring VLM at the tide  
119 gauge. However, they have not used them as a dedicated geodetic tie between a cGPS and the  
120 tide gauge, as we propose and test here.

121         We describe experiments using five integer years of SAR acquisitions from the  
122 German Aerospace Center's (DLR's) TerraSAR-X (TSX) satellite mission over a test site  
123 containing the Fremantle (FREM) and Hillarys (HILS) tide gauges in Perth (Australia). These  
124 tide gauges are suitable for this experiment because (1) HILS has a co-located cGPS (fixed to  
125 the tide gauges structure) that can be used for validation, (2) FREM has a long running (>100  
126 year) tide gauge record, and (3) the tide gauges are only ~30 km apart, so can be used to test  
127 the differential VLM between them on the assumption that the SLC signal at both tide gauges  
128 are the same. HILS is known to be undergoing non-linear VLM (Featherstone et al. 2015),  
129 while Featherstone et al. (2015) has suggested FREM is also undergoing non-linear VLM (cf.  
130 Thompson and Merrifield 2018; Burgette et al. 2013).

131 Other SAR scenes are available over the test site, e.g., C-band scenes from the  
132 European Space Agency's Envisat and Sentinel-1 satellite missions, but neither provide a  
133 sufficiently long time series nor the number of scenes that we have available from TSX. For  
134 example, Sentinel-1A started acquisitions in 2014 and observed the test site for an eight  
135 month period (e.g., Parker et al. 2017), while Sentinel-1B did not begin observations until  
136 2016. Comparisons between X-band and C-band displacements in Parker et al. (2017)  
137 indicated reasonable agreement between these data although over a very short period, so are  
138 not conclusive. Using 141 TSX scenes acquired between 7 October 2012 and 7 October 2017  
139 (herein referred to by decimal years 2012.8-2017.8 to denote five integer years), we have  
140 estimated VLM rates at these tide gauges in the test site to determine the utility of InSAR to  
141 monitor differential VLM between tide gauges and cGPS stations as an alternative to  
142 differential levelling for the geodetic tie.

143 Repeat differential levelling and InSAR are two different relative measurement  
144 techniques: levelling measures multiple short-distance (maximum of ~40 m sight length)  
145 height differences from ground-based instruments set up orthogonal to the local gravity  
146 vector (e.g., Vaníček et al. 1980), while InSAR measures the geometric off-nadir LoS using  
147 radar backscatter from the Earth's surface back to the satellite (see e.g., Hanssen 2001) from  
148 repeat orbits (e.g., 11 days for TSX). Hence, repeat levelling measures the height difference  
149 between specific points on land during separate surveys (ideally four times per year for VLM  
150 monitoring) with respect to the local gravity vector, but InSAR measures the changes in LoS  
151 range between the ground (over a 'pixel', not a specific point) and the satellite for multiple  
152 pixels within the scene (50 km x 30 km for TSX stripmap). The processed InSAR LoS  
153 ranges, and repeat levelling surveys produce displacement time series, but at different spatial  
154 and temporal resolution with their own specific measurement and error characteristics. Both

155 time series can be used to estimate rates of VLM at tide gauges, relative to a cGPS station, as  
156 we demonstrate for InSAR.

157 Mahapatra et al. (2018) used a radio transponder co-located at a tide gauge in the  
158 Netherlands to determine InSAR VLM rates relative to the tide gauge and co-located cGPS.  
159 However, tide gauge co-located InSAR ground infrastructure, such as transponders and  
160 corner reflectors (CRs) are not available at most global tide gauges, all of which need  
161 monitoring for VLM to estimate accurate rates of SLC. Indeed, Wöppelmann and Marcos  
162 (2016) report that only 14% of the Global Sea Level Observing System (GLOSS) tide gauges  
163 have co-located cGPS stations (i.e., fixed directly to the tide gauge structure), so that  
164 differential VLM for the tide gauges where cGPS is not co-located will need to be monitored.  
165 While the use of transponders and CRs may provide improved location accuracy (e.g.,  
166 Mahapatra et al., 2014; Dheenathayalan et al. 2016; 2017; Garthwaite 2017), these are not  
167 likely to be available on a global scale for some years, and perhaps never for countries that  
168 cannot afford such infrastructure. Hence, we test differential InSAR to tide gauges as an  
169 alternative technique that could potentially be applied globally, depending on the availability  
170 of SAR imagery.

171

## 172 **2. Methods and data**

173 The data used and processing methods described in this section are arranged with a sub-  
174 section for each technique. The cGPS in the test site (International GNSS Service (IGS) code  
175 PERT; Figure 1), is used to transform the InSAR displacement time series to a terrestrial  
176 reference frame (TRF) – IGS08 for this experiment – which is aligned with the International  
177 reference Frame 2008 (ITRF2008; Altamimi et al. 2011). Derived TSX IGS08 rates can then  
178 be compared to cGPS IGS08 rates at other locations for validation, and the TSX rates at each  
179 tide gauge are then in a known TRF.

180 We use PERT as the single reference point because it is considered the most reliable  
181 site for (1) cGPS time series (since 1995) and (2) the TSX reference pixel nearest to the  
182 cGPS. This is compared to HIL1 which is co-located with HILS but located on the roof of the  
183 tide gauges shed on a jetty in a boat harbour full of moored yachts with tall masts (possibly  
184 causing multipath) and has a break in its time series (Figure 2B). CUIAI is mounted atop a 4-  
185 story building, which may not be stable, nor a reliable site for TSX backscatter from the  
186 cGPS location.

187

## 188 **2.1 InSAR**

189 We first processed the 141 TSX scenes using the small baseline multi-temporal InSAR (MTI)  
190 method implemented in the Stanford Method of Persistent Scatterer (StaMPS; Hooper et al.  
191 2012) software as described in Hooper (2008). The interferograms were processed using  
192 Doris (Delft object-oriented radar interferometric software; Kampes and Usai 1999), forming  
193 705 small baseline interferograms. The small baselines interferogram pairs were selected  
194 manually, with the objective of keeping perpendicular (i.e., the distance between repeat  
195 satellite positions, orthogonal to the LoS) and temporal baselines as small as possible, but  
196 retaining redundancy in the network so that each scene was connected by at least three small  
197 baseline interferograms.

198 The high redundancy small baselines help reduce the effect of temporally variable  
199 tropospheric noise (Williams 1998; Agram and Simons 2015; Fattahi and Amelung 2015;  
200 Cao et al. 2018). Residual time correlated noise in the TSX time series was identified and  
201 accounted for in the time series analysis in section 3.2. The TSX phase ramp was estimated  
202 and used to remove the long-wavelength orbit and ionosphere effects that may be present in  
203 the TSX scene extent of 50 km x 30 km. This is appropriate for extents of <100 km (Hooper  
204 et al. 2012), but also because X-band is less affected by the ionosphere (cf. Gomba et al.

205 2017), TSX orbit errors are relatively small (Fattahi and Amelung 2014), and the study area  
 206 is relatively flat, so less affected by stratified tropospheric effects (Bekaert et al. 2015).

207 The TSX slowly-decorrelating filtered phase (SDFP; Hooper 2008) pixels (stripmap  
 208 spatial resolution  $\sim 3$  m) were down-sampled to 30 m spatial resolution, using the method of  
 209 Hooper et al. (2012), resulting in 827,215 points. The pixels were down-sampled to reduce  
 210 the computing load and smooth noisy pixels, and were calculated using nearby pixels  
 211 weighted from their signal-to-noise ratio (Hooper et al. 2012). We conducted earlier  
 212 experiments with the individual TSX SDFP pixels for the 4-year 2012.7-2016.7 time series  
 213 (10,175,104 versus 728,702 down-sampled pixels), which indicated that the rates from the  
 214 down-sampled pixels were more reliable when tested with independent results (i.e., cGPS and  
 215 altimetry minus tide gauge VLM rates). For this reason, the down-sampled pixels were used  
 216 in this experiment, and referred to herein as DPs. The TSX phase differences were  
 217 unwrapped using 3D phase unwrapping (Hooper et al. 2007), and initially relate to an  
 218 arbitrary datum where the mean of all velocities is taken as the zero reference.

219 The small baseline  $m \times n$  array comprises unwrapped DP phase differences ( $\Delta\phi$ ),  
 220 where  $m$  is the number of DPs (827,215) and  $n$  is the number of small baseline  
 221 interferograms (705). To compute relative displacements for each DP per scene acquisition  
 222 ( $t_a$ ), which is 140 for this time series (first column of 141 scenes is removed; see below), a  
 223 coefficient matrix  $\mathbf{G}$  ( $n \times p$ ) is formed that describes the functional relation between the small  
 224 baseline interferograms and the number ( $p$ ) of  $t_a$  (705  $\times$  140). The vector of phase  
 225 displacements  $\mathbf{d}$  for each DP is computed row by row, where  $\Delta\phi = \mathbf{G}\mathbf{d}$  using Gaussian  
 226 elimination to invert the matrix. Each successive computation of  $\mathbf{d}$  builds the  $m \times p$   
 227 displacement matrix  $\mathbf{D}$ . To remove the rank defect from  $\mathbf{G}$ , the first column is removed  
 228 (leaving 140 from 141 scenes) so that the first acquisition becomes  $t_0$  and is the zero  
 229 reference for the time series of displacements. This means that the TSX time series

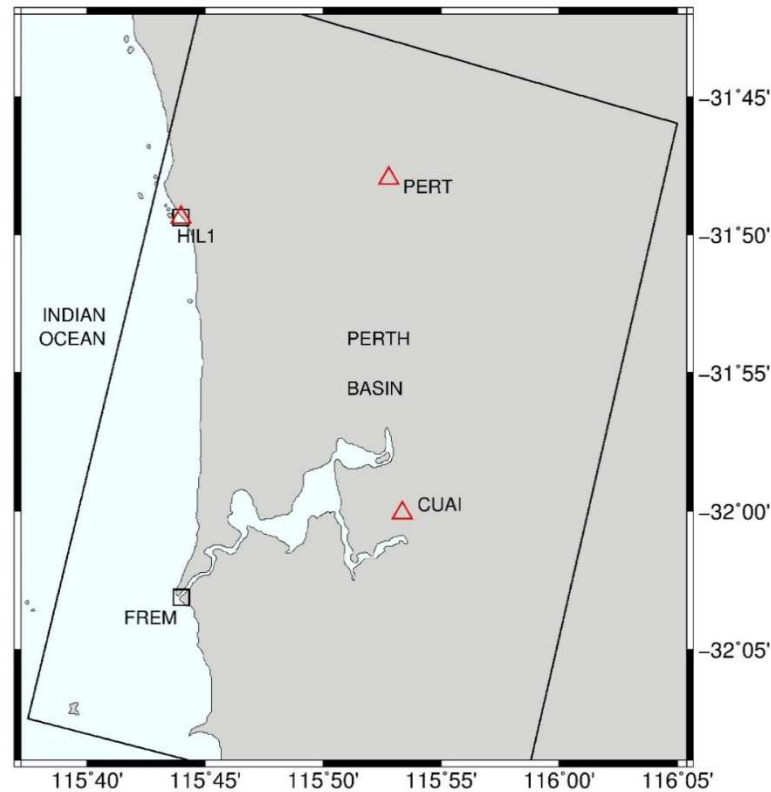
230 displacements will be relative to zero, so that although the displacement trends are  
231 transformed relative to the IGS08 reference frame, TSX DPs do not become IGS08 heights.  
232 The  $D_{m,p}$  (827,215 x 140) displacement array is transformed to the TRF as per section 2.5.

233

## 234 **2.2 GPS**

235 Daily cGPS positions were obtained from the Nevada Geodetic Laboratory (NGL;  
236 <http://geodesy.unr.edu/NGLStationPages/GlobalStationList>; Blewitt et al. 2018). These data  
237 were used to estimate time series velocities and realistic uncertainties using the CATS  
238 software (Williams 2008). The spectral index was solved for the five-year TSX period  
239 (2012.8-2017.8) using 11 cGPS receivers located on a building at Curtin University in  
240 addition to PERT (pillar mounted) and HIL1 (co-located with HILS). The average spectral  
241 index was  $-0.72$  for all 13 cGPS time series, so this fixed spectral index was used to  
242 recompute the trend with the annual and semi-annual terms and variable white noise. The  
243 mean spectral index from all 13 cGPS time series was used to avoid introducing a bias in the  
244 spectral indices at PERT and HIL1 that could have resulted from the shorter variable time  
245 series. Only one of these building-mounted cGPS (CUAI; Figure 1) was used to provide an  
246 additional cGPS comparison for the TSX, because it had the best quality time series (Figure  
247 2C), while the others were all fixed to the same building, and some had incomplete and/or  
248 gaps in their time series for the full TSX time period.

249



250  
251



252

253 Figure 1: (Top) Map showing the test site, with cGPS stations (red triangles) and tide gauges

254 (black squares), with the extent of the TSX scene shown by the black line. cGPS CUAI is

255 located on top of a multi-storey building. (Bottom) FREM tide gauge (left), and HIL1 co-

256 located cGPS and HILS tide gauge (right) are shown in the red circles. Bottom images

257 sourced from Google Imagery (2019).

### 258 *2.3 Tide gauge sea level*

259 Monthly mean sea level values from the Permanent Service for Mean Sea Level

260 (PSMSL, Holgate et al 2013) were used for 1993.0–2018.0 (altimeter period) and for 2012.8–

261 2017.8 (TSX period) to compare InSAR VLM rates to (1) tide gauge minus altimetry VLM at  
262 HILS and FREM, and (2) to differential tide gauge minus altimetry VLM rates between these  
263 gauges. HILS and FREM are ~30 km apart (Figure 1), where any difference in SLC is  
264 assumed to be due to relative tide gauge VLM (e.g., Burgette et al. 2013), so this will be used  
265 to provide some additional evidence to support the TSX differential VLM (but not absolute  
266 VLM in the IGS08 TRF). In creating the gridded altimeter product, a dynamic atmosphere  
267 correction has been applied by AVISO. This accounts for the inverse barometer effect at all  
268 periods, and for barotropic ocean dynamics at periods shorter than 20 days. For consistency  
269 among the tide gauge and altimetry data, the same correction was also applied to each of the  
270 tide gauge time series, as extracted from the nearest grid point of the ocean model output. The  
271 effect of long period tides (Woodworth, 2012) was found to be below 0.03 mm/yr and was  
272 thus neglected.

273 The CATS software was first used to estimate rates and uncertainties for the full sea  
274 level records at both tide gauges as a check on the results and data. The power law index was  
275  $-0.96$  for the full ( $>100$  year) FREM record, indicating flicker noise. Similar results were  
276 obtained for HILS, with a power law index of  $-1.14$  for the full ( $\sim 25$  year) record. To avoid a  
277 possible bias in the sea level rates from using a spectral index computed from a short period  
278 time series, the five-year rates were recomputed in CATS with the power law index fixed at  
279  $-0.96$ , on the assumption that the true spectral index of two tide gauges close together should  
280 be very similar.

#### 281 ***2.4 Altimetry sea level***

282 To compare the InSAR-derived VLM, tide gauge sea level observations minus  
283 satellite altimetry observations near the tide gauge can be used to estimate VLM at the tide  
284 gauge (e.g., Pfeffer and Allemand 2016; Wöppelmann and Marcos 2016, and many others).  
285 Altimetry data from AVISO (the Ssalto/Duacs, delayed mode, gridded absolute dynamic

286 topography product using all available satellites, and with a dynamic atmosphere correction  
287 applied as described above) was used to estimate monthly sea surface heights adjacent to the  
288 two tide gauges. Data were extracted from the grid point within 200 km of the tide gauge  
289 which explains most of the variability seen at the tide gauge. This is a compromise, designed  
290 to limit the effect of increased instrumental and sampling errors near the coast, balanced  
291 against the inevitable loss of some near-coastal signal, and inevitable (and time dependent, as  
292 the satellite systems evolve over time) limitation of the satellite measurement system. Tide  
293 gauge sea level monthly means were subtracted from altimetry monthly means with the VLM  
294 rates estimated using CATS from the differenced time series for the full altimeter record  
295 (1993.0-2018.0) and for the TSX period (2012.8-2017.8), after accounting for annual and  
296 semi-annual terms. This method assumes that, apart from any seasonal cycle, altimetry sea  
297 level realises the ‘true’ SLC rate at the tide gauge, with the difference to tide gauge sea level  
298 interpreted as the VLM at the tide gauge, with other errors (e.g., altimetry observation and  
299 processing errors) assumed negligible. Wöppelmann and Marcos (2016) estimated global tide  
300 gauge minus satellite altimetry uncertainties of up to  $\pm 3$  mm/yr, but with a median of  $\pm 1$   
301 mm/yr from a set of 478 selected global tide gauges.

302

### 303 ***2.5 Transformation of InSAR time series to TRF***

304 Transforming the TSX LoS rates into a TRF is important so that the rates from different  
305 measurement techniques (i.e., GPS, InSAR and altimetry) can be directly compared (cf.  
306 Wöppelmann et al. 2007; Bekaert et al. 2017; Hammond et al. 2018; Mahapatra et al. 2018).  
307 Using the S-transform method from Mahapatra et al. (2018) for a large data set, the  $\mathbf{I}$  matrix  
308 ( $m \times m$ ) becomes large, and we found the  $m = 827,215$  array to be beyond available computer  
309 memory. An alternative method was therefore implemented, where the TSX reference point  
310 (RP) displacement row vector  $\mathbf{d}_{RP}$  is subtracted from all  $\mathbf{d}_i$ , (DP displacement vectors held in

311 the displacement matrix  $\mathbf{D}$  ) where  $\mathbf{d}_{RP}$  is given a (temporary) arbitrary zero displacement for  
 312 all acquisition times ( $t_a$ ). This produces the same results as the S-transform method but is  
 313 done as a direct operation on  $\mathbf{D}$  and does not require the computation of the large  $\mathbf{I}$ .

314 The  $\mathbf{d}_i$  are then transformed to the TRF through the connection between  $\mathbf{d}_{RP}$  and the  
 315 cGPS time series, which are treated as co-located (cf. Figure 2A). The velocity is computed  
 316 from the cGPS time series (Section 2.2) for the same period as the InSAR  $\mathbf{d}_{DP}$  (2012.8-  
 317 2017.8) so that the  $\mathbf{d}_i$  time series transformed as (Mahapatra et al. 2018)

$$318 \quad \mathbf{d}_{i,TRF} = \mathbf{d}_i + \mathbf{H}\mathbf{d}_{GPS} \quad (1)$$

319 where  $\mathbf{d}_{i,TRF}$  is  $\mathbf{d}_i$  related to the TRF.  $\mathbf{H}$  is a vector constraint to set the datum of a free  
 320 network (here comprising ones whereby the average of all displacements is taken as the  
 321 reference) and  $\mathbf{d}_{GPS}$  is the vector of linear displacements at each TSX  $t_a$  from the estimated  
 322 cGPS trend connecting the InSAR DPs to the TRF computed as

$$323 \quad \mathbf{d}_{GPS} = v_{GPS} \times (t_a - t_0)/365.25 \quad (2)$$

324 where  $v_{GPS}$  is the estimated linear velocity of the cGPS time series in mm/yr and  $(t_a - t_0)$  is  
 325 the period (days) over which  $v_{GPS}$  is computed, then converted to years by dividing by  
 326 365.25. The resulting displacement array  $\mathbf{D}_{TRF}$  comprises row vectors  $\mathbf{d}_{i,TR}$  representing  
 327 each DP displacement transformed into the TRF. The TSX rate and uncertainty can then be  
 328 computed from  $\mathbf{d}_{i,TRF}$  at the tide gauge locations.

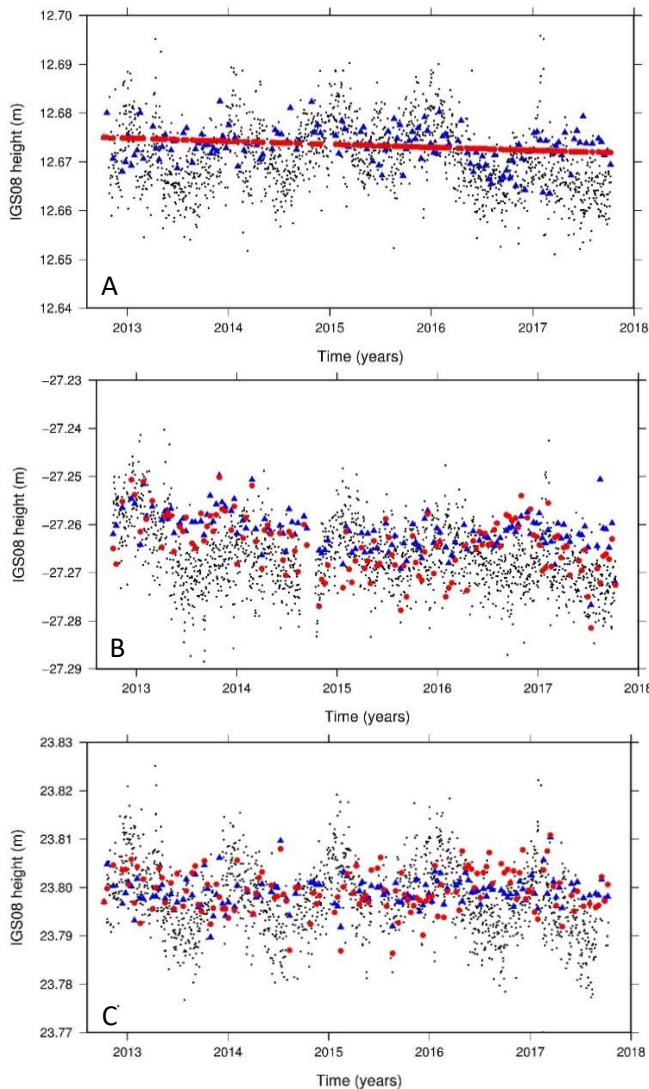
329

### 330 **3. Results and Discussion**

#### 331 **3.1 Time series comparisons**

332 Initial comparisons were made between the cGPS and TSX time series as a check. Figure 2  
 333 shows the cGPS time series at PERT, HIL1 and CUA1 compared to their nearest TSX DP  
 334 before and after transformation to IGS08 constrained to the CATS-estimated cGPS IGS08  
 335 rate at the RP (PERT). The linear rate (red dots in Figure 2A) represents the transformed TSX

336 rate, which is now coincident with the cGPS rate. The pre-transformation TSX time series  
 337 (blue triangles) indicates that it is sensing similar VLM signals to the cGPS. The main  
 338 differences are between the maximum amplitude of the cGPS annual periodic signal, where  
 339 the TSX amplitudes are, generally lesser magnitude. This may be due to the different  
 340 measurement and processing characteristics of the SAR and GPS systems. For instance, the  
 341 TSX may be sensing a close-by, but different, feature to the cGPS structure, and also the  
 342 filtering in the TSX processing may tend to over-smooth the seasonal amplitude when  
 343 compared with the higher solution rate of the cGPS.



344

345

346

347

348

Figure 2: (A) PERT cGPS (IGS08) time series (black dots) compared to the time series for  
 the nearest TSX LoS DP before transformation (blue triangles) and after transformation (red

349 circles). (B) As for (A), but for HIL1 cGPS time series and nearest TSX LoS DP before and  
350 after the rates have been transformed; (C) As for (B), but for CUIAI cGPS time series and  
351 nearest TSX LoS DP. Note that the cGPS time series daily solutions are IGS08 heights, but  
352 the TSX time series displacements are relative to zero, shifted on the y-axis to IGS08 heights  
353 for plotting purposes to compare to the cGPS time series.

354

355 Both the TSX and GPS time series in Figure 2A suggest an uplift trend until 2016,  
356 and then possibly subsiding after this, although this should be viewed cautiously for a  
357 relatively short time series, and in the presence of the GPS seasonal signal. The HILS TSX  
358 and HIL1 GPS time series in Figure 2B do not agree as well as at PERT, although there are  
359 still similarities between them. HIL1 is a ‘noisier’ site than PERT (which is why PERT was  
360 used as the reference point for the TRF), for both GPS and the TSX. because of the masts on  
361 yachts moored nearby, and also because the TSX may not be sensing the tide gauge location  
362 exactly (cf. Figure 1). Similar problems may be experienced at some global tide gauges  
363 where this method may be applied.

364 The rate for the cGPS station (CUIAI) located on top of a multi-storey building at  
365 Curtin University (Figure 1C) was also estimated as an additional comparison on the TSX.  
366 Because a site on a building is not ideal due to possible building movement (e.g., thermal  
367 expansion and contraction), and that the TSX DP may not sense the same position on the  
368 building as the cGPS, it was used only as a check on the TSX VLM rates.

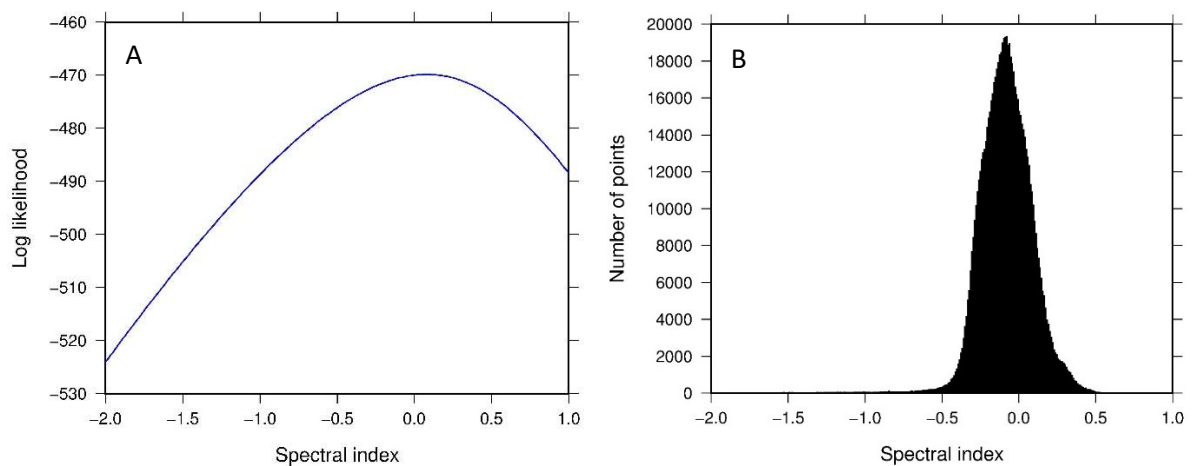
369

### 370 ***3.2 InSAR noise analysis***

371 The noise content in the residual TSX time series (following processing) is not known and  
372 likely to be time-correlated. If unaccounted for it may introduce errors in the VLM rate and  
373 certainly underestimate the rate uncertainty (Williams et al. 1998; Williams 2003; 2008). We

374 conducted an analysis of the time correlated noise in the TSX time series so that a more  
 375 appropriate noise model could be applied to the estimation of the rate and rate uncertainty).  
 376 The relatively short time series of five years and 141 epochs limits the number of resolvable  
 377 parameters in the maximum likelihood estimation (MLE) so we used a power-law only model  
 378 instead of a power-law plus white noise model more typically used in geophysical time series  
 379 analysis. It is more important to capture the coloured noise aspects of the series than the  
 380 white noise since this is what influences the rate uncertainty the greatest. We took a network-  
 381 based approach where all 827,215 DPs in the SAR scene were included in to estimate the  
 382 spectral index on the assumption that the TSX time series noise characteristics are the same  
 383 across the scene and therefore provide a more robust estimate of the spectral index. To reduce  
 384 the computational burden, a single covariance matrix was precomputed and applied to all  
 385 827,215 DP time series in the image. A log-likelihood (LL) calculation was run on a range of  
 386 spectral indices from  $-2$  (random walk) to  $+1$  (at 0.1 intervals) for all DP time series to find  
 387 the maximum LL (Figure 3A) and then interpolated to get the best estimate of the spectral  
 388 index for each DP time series.

389



390

391 Figure 3: (A) is the log-likelihood (LL) for TSX DP #1 as a function of spectral index. The

392 estimated spectral index is calculated from the largest LL and the two values either side. (B)

393 Histogram of spectral indices for each transformed TSX DP time series.

A: Simulated Spectral Index	B: Estimated Spectral Index
0.00	$0.19 \pm 0.19$
-0.09	$0.10 \pm 0.18$
-0.26	$-0.08 \pm 0.18$
-0.50	$-0.33 \pm 0.18$
-1.00	$-0.85 \pm 0.17$

394

395 Table 1: Simulated fixed spectral index (column A) and spectral index estimated as the  
 396 standard deviation of all DP time series in the TSX data (column B).

397

398

399

400

401

402

403

404

405

406

407

408

409

410

### 411 **3.3 Sea level rates**

412

413

414

415

416

The spectral indices of all 827,215 DP time series is shown in Figure 3B, with a mean value of  $-0.09$ . The estimated spectral index from this five-year time series may be biased on the low side (lesser magnitude, but negative value) because we remove a component of the correlated signal together with the “true” slope when the slope is estimated. To test for a possible bias, we simulated noise with a fixed spectral index and the same number of points in the TSX data, then estimated the spectral index (Table 1, column A). The test indicates the true spectral index from the data is likely to be larger in magnitude (but negative) than that estimated and shown in Table 1. The range (highest to lowest) of the simulated estimates is similar to those computed from the data ( $\sim 1.0$ ), so from Table 1 we adopt the estimated spectral index value of  $-0.08$  (closest to the computed value of  $-0.09$ ) which is then related to the corresponding simulated spectral index of  $-0.26$ . A fixed spectral index of  $-0.26$  is then used in CATS for all TSX rate estimation.

Linear rates of SLC from the tide gauges and altimetry for 1993.0-2018.0 and for the TSX period 2012.8-2017.8 are shown in Table 2. The 1993.0-2018.0 SLC rates are included as a comparison, with the shorter period being more affected by variability in short term sea level (Woodworth et al. 2019). The short-term relative sea level rates are of less interest in this study, but the differential rates between the tide gauge sites are used to support the validity of

417 the TSX VLM (Section 3.4). The tide gauge rates contain VLM that is dependent on the tide  
 418 gauge site, and also the sea level signal. The altimetry measures only sea level at a location  
 419 offshore from the tide gauge. Over a distance of only ~30 km, the sea level rate should be the  
 420 same, as seen by the altimetry over the longer 1993.0 – 2018.0 period, so that the differential  
 421 rate between the tide gauges is assumed to be primarily VLM. The tide gauge differential rate  
 422 sums to ~47 mm over ~25 years, which compares to ~70 mm over 40 years in Featherstone et  
 423 al. (2015) from repeat levelling. Both show HIL1 subsiding at a faster rate than FREM.

424

	SLC 1993.0-2018.0 (mm/yr)	SLC 2012.8-2017.8 (mm/yr)
<b>FREM</b>		
Tide gauge	+6.95±2.66	-11.90±9.67
Altimetry	+5.23±2.47	-14.52±9.77
<b>HILS</b>		
Tide gauge	+8.84±2.58	-13.96±10.04
Altimetry	+5.29±2.51	-18.49±9.48

425

426 Table 2: Tide gauge and altimetry sea level rates for FREM and HILS. The tide gauge rates  
 427 contain the VLM and the ocean sea level signal, whereas the altimetry contains only the sea  
 428 level ocean signal.

429

430 All VLM rates were computed using CATS, as described in Sections 2.2, 2.3 and 3.2.

431 The tide gauge minus altimetry VLM rates were estimated from the differenced monthly  
 432 means (as per Section 2.4) so are slightly different to the differences of the rates shown here.

433 The differential tide gauge minus altimetry VLM rate between the tide gauges was also  
 434 estimated from the double differences of the tide gauge and altimetry monthly means, which  
 435 resulted in reduced uncertainties to those shown in Table 2. Double differencing was used  
 436 only for the tide gauge and altimetry sea level measurements because the ocean contains large  
 437 annual, interannual and decadal variabilities to which linear rates can be more sensitive than  
 438 GPS and TSX rates.

439 **3.4 VLM rates**

440 The small baseline LoS phase differences were converted to VLM displacements for each DP  
441 on the assumption that there is no relative horizontal motion among the cGPS and tide gauges  
442 (indicated to be the case for this test site in Parker et al. 2017). All DP time series  
443 displacements were then referenced to the TRF at the cGPS (PERT) using the methods  
444 described in Section 2.5. Equations (1) and (2) were used to transform to the TRF through the  
445 connection to the cGPS, using  $v_{GPS} = -0.62 \pm 0.52$  mm/yr for PERT in the TRF. This cGPS  
446 rate was estimated using CATS for 2012.7-2017.7 as per Section 2.2.

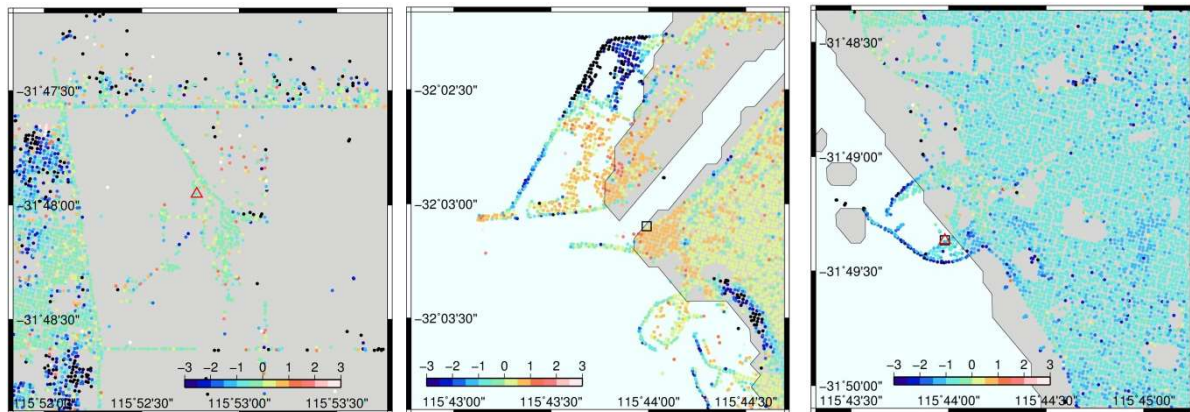
447 The TSX rates were computed in CATS using the fixed spectral index of  $-0.26$   
448 estimated in Section 3.2, variable white noise and annual and semi-annual terms. These rates  
449 are shown in Figure 4, with Figure 4A showing DPs close to the cGPS (RP used is calculated  
450 within 4 m) with rates between  $-0.5$  mm/yr and  $-1.0$  mm/yr (RP fixed to  $-0.62$  mm/yr). This  
451 indicates that the land surrounding the cGPS is subsiding at a similar rate to the cGPS  
452 structure so that it is reasonable to adopt the closest DP as TSX RP in this case and supports  
453 PERT's use as the RP for the TRF transformation.

454 Figure 4B shows the region adjacent to FREM to be uplifting in the range  $+0.5$  mm/yr  
455 to  $+1.0$  mm/yr, but the location of the tide gauge itself is in the  $0.0$  mm/yr to  $+0.5$  mm/yr  
456 range (FREM  $+0.45$  mm/yr). The area showing the higher uplift is covered by several  
457 buildings, so these may be the dominant scatterers near this location. The subsidence  
458 experienced by the coastal breakwater structure to the north of FREM is notable, as is the  
459 area along the waterfront to the south. These comprise human-made structures that are liable  
460 to settlement and subsidence. The areas without DPs are likely due to temporal decorrelation,  
461 from vegetation changes or in the car parks and vehicle unloading/storage area on the docks  
462 where the position and cars will not be the same for each SAR acquisition. The VLM in the  
463 vicinity of Fremantle is variable, ranging from  $+2$  mm/yr to  $<-3$  mm/yr which reinforces the

464 need to monitor VLM at the tide gauge site, rather than simply adopt the rates from a remote  
 465 cGPS station that is not co-located with the tide gauge.

466 The DPs near HIL1 and HILS (Figure 4C) also indicates consistency in the  $-1$  mm/yr  
 467 to  $-1.5$  mm/yr range (HIL1 TSX rate at  $-1.20$  mm/yr), which supports the adoption of the  
 468 nearest DP. It is not clear if the DP adopted is actually sensing the tide gauge itself or the  
 469 close by land (within  $\sim 5$  m), but they do appear to be subsiding at similar rates.

470



471

A

B

C

472 Figure 4: TSX DP rates (mm/yr) around (A) PERT (red triangle); (B) FREM (black square);  
 473 (C) HIL1 (red triangle), and co-located HILS tide gauge (black square).

474

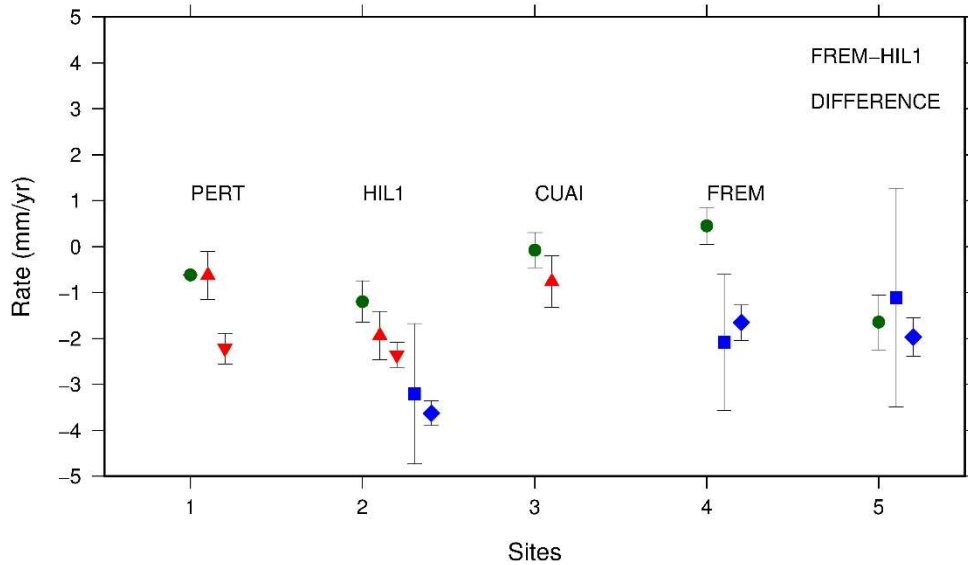
475 The VLM rates from the different measurement techniques are summarised in Figure  
 476 5, and listed in Table 3. The difference between the 2012.8-2017.8 cGPS rates (red triangles)  
 477 and the TSX rates (green circles) at HIL1 (cGPS  $-1.94 \pm 0.53$  mm/yr; TSX  $-1.20 \pm 0.40$   
 478 mm/yr) and CUA1 (cGPS  $-0.78 \pm 0.60$  mm/yr; TSX  $-0.08 \pm 0.38$  mm/yr) indicate the precision  
 479 of the TSX within the TRF. Although the agreement is at the edge of the respective error bars  
 480 computed for the TSX time series (Figure 5), the differences are  $< 0.74$  mm/yr, so less than  
 481 the median uncertainty of  $\pm 1$  mm/yr for altimetry minus tide gauge VLM from the global  
 482 study of Wöppelmann and Marcos (2016). The CATS-derived cGPS rates are both less than  
 483 the CATS-derived TSX rates (larger subsidence for GPS), which indicates a bias, although

484 this cannot be certain for only two cGPS stations, one of which is building-mounted. The  
485 TSX at FREM suggests small uplift of  $+0.45 \pm 0.40$  mm/yr, which is barely significantly  
486 different from zero VLM (cf. Burgette et al. 2013), but this is inclusive to the 2012.8-2017.8  
487 period only, and care should be taken in making direct comparisons with VLM rates from  
488 different periods, especially as some parts of the Perth Basin have experienced non-linear  
489 subsidence (Featherstone et al. 2015).

490 It should also be considered that the uncertainties shown in Table 3 contain only the  
491 TSX time series uncertainty at the site, so does not fully account for uncertainties in the cGPS  
492 and TSX at the PERT RP, and the cGPS in the comparisons at HIL1 and CUIAI. A linear  
493 error propagation may provide an upper bound approximation of the uncertainty if all the  
494 related measurements are taken into account. Using the time series uncertainties in Table 3  
495 for the PERT TSX (nominally zero) and cGPS, we propagate these to the FREM TSX rate,  
496 getting  $\pm 0.69$  mm/yr, while for HIL1 we obtain  $\pm 0.87$  mm/yr, and CUIAI  $\pm 0.88$  mm/yr. The  
497 CUIAI and HIL1 sites include their cGPS uncertainty in the linear error propagation. These  
498 may be an upper bound, but suggest that the differences between cGPS and TSX at HIL1 and  
499 CUIAI are within the uncertainty when the TRF RP is taken into account.

500 Longer period cGPS rates are shown in Table 4 that were computed using CATS and  
501 NGL data for this study (shown in Figure 5), and also from the University of La Rochelle  
502 processing (ULR6A, Santamaría-Gómez et al. 2017) and the Median Interannual Difference  
503 Adjusted for Skewness (MIDAS) method (Blewitt et al. 2016). These are shown to provide  
504 an additional comparison for the longer term cGPS and altimetry minus tide gauge VLM  
505 rates thus serving as (1) a check for the other rates of similar periods, and (2) give an  
506 indication whether there is non-linearity at the VLM at these sites when compared to different  
507 time periods.

508



509  
510

511 Figure 5: Velocity estimates (mm/yr) for TSX 2012.8-2017.8 (green circles), GPS 2012.8-  
512 2017.8 (red triangles); longer term (see Table 4) cGPS rates computed for this study using  
513 NGL data (inverted red triangles), and tide gauge minus altimetry VLM 2012.7-2017.7 (blue  
514 squares) and 1993.0-2018.0 (blue diamonds). So-called ‘Site’ 5 actually shows the  
515 differential VLM between HILS and FREM for TSX and tide gauge minus altimetry. See  
516 Table 3 for numerical VLM rates.

517  
518

519 The tide gauge minus altimetry VLM rates for 2012.8-2017.8 are  $-2.09 \pm 1.48$  mm/yr  
520 and  $-3.21 \pm 1.53$  mm/yr (Table 3) for FREM and HILS, respectively, and appear to be  
521 systematically larger subsidence rates than the TSX ( $\sim 2$ - $2.5$  mm/yr more subsidence;  
522 referenced to IGS08 at the PERT cGPS). These differences are statistically significant, and  
523 also larger than the  $\pm 1$  mm/yr uncertainty estimate for tide gauge minus altimetry VLM from  
524 Wöppelmann and Marcos (2016), suggesting that the constant offset may be a systematic bias  
525 between the IGS08-referenced TSX and the tide gauge minus altimetry VLM. The cGPS  
526 rates at HIL1 and CUA1 are closer to the TSX ( $\sim 0.74$  mm/yr) than the altimetry minus tide  
527 gauge VLM at HILS ( $\sim 1.2$  mm/yr), suggesting that the TSX is slightly closer to the true  
VLM rate, albeit on the assumption that cGPS is the most reliable technique for determining

528 VLM. In this comparison, the differential TSX is referenced to cGPS at PERT, so can be  
 529 directly compared to cGPS processed in the IGS08 reference frame.

Site	TSX 2012.8-2017.8	cGPS 2012.8-2017.8	Alt-tide gauge 2012.8-2017.8	Alt-tide gauge 1993.0-2018.0
PERT	$-0.62 \pm 0.00(2)$	$-0.62 \pm 0.52$		
HIL1/HILS	$-1.20 \pm 0.45$	$-1.94 \pm 0.53$	$-3.21 \pm 1.53$	$-3.63 \pm 0.26$
CUAI	$-0.08 \pm 0.38$	$-0.78 \pm 0.60$		
FREM	$+0.45 \pm 0.40$		$-2.09 \pm 1.48$	$-1.66 \pm 0.38$
HILS – FREM difference	$-1.65 \pm 0.60$		$-1.12 \pm 2.38$	$-1.97 \pm 0.42$

530  
 531 Table 3: Multi-technique VLM rates for each site (including HILS – FREM VLM  
 532 difference). All units are mm/yr.

533  
 534 To investigate the possible non-linearity of VLM at these sites, we have shown  
 535 longer term (1993.0-2018.0) rates for altimetry minus tide gauge (Table 3) and cGPS VLM  
 536 (various periods; Table 4)., These are also plotted in Figure 5, and suggest that the rates  
 537 shown here are dependent on the time period used, indicating non-linearity (cf. Burgette et al.  
 538 2013; Merrifield and Thompson 2018). This is most evident at PERT, where the 2012.8-  
 539 2017.8 cGPS rate is  $-0.62 \pm 0.52$  mm/yr (Table 3), but for 1996.0-2019.3 (Table 4) is –  
 540  $2.22 \pm 0.33$  mm/yr computed using CATS for this study (from NGL data), which is in  
 541 reasonable agreement with  $-2.09 \pm 0.38$  (1995.0-2014.0) for ULR6 (Santamaria-Gomez et al.  
 542 2017) and  $-2.34 \pm 0.59$  (1996.0-2019.3) for MIDAS (Blewitt et al. 2016). Non-linearity is less  
 543 obvious at HIL1 ( $-1.94 \pm 0.53$  mm/yr compared to  $-2.36 \pm 0.27$  mm/yr for 1996.0-2019.3),  
 544 although this location has been shown by Featherstone et al. (2015) to have undergone non-  
 545 linear subsidence due to increased groundwater extraction in the early 2000s. We computed  
 546 HIL1 cGPS rates as  $-2.36$  mm/yr using CATS and NGL data, compared to  $-2.78 \pm 0.31$  mm/yr  
 547 (2005.0-2014.0) for ULR6 (Santamaria-Gomez et al. 2017) and  $-2.69 \pm 0.62$  mm/yr (1997.7-  
 548 2019.3) from MIDAS (Blewitt et al. 2016).

549

Site	cGPS (mm/yr)
PERT (NGL) 1996.0-2019.3	$-2.22 \pm 0.33$
PERT (ULR6) 1995.0-2014.0	$-2.09 \pm 0.38$
PERT (MIDAS) 1996.0-2019.3	$-2.34 \pm 0.59$
HIL1/HILS (NGL) 1996.0-2019.3	$-2.36 \pm 0.27$
HIL1 (ULR6) 2005.0-2014.0	$-2.78 \pm 0.31$
HIL1 (MIDAS) 1997.7-2019.3	$-2.69 \pm 0.62$

550

551 Table 4: Longer period rates for cGPS stations from NGL time series processed for this study  
 552 in CATS, ULR6 (Santamaría-Gómez et al. 2017) and MIDAS (Blewett et al. 2016) .

553

554 The tide gauge minus altimetry VLM for the TSX period (2012.8 – 2017.8) is not  
 555 statistically different to the 1993.0-2018.0 period, although this is partly due to the larger  
 556 uncertainty in the TSX-period VLM. The difference between long-term HIL1 ( $-2.36 \pm 0.27$   
 557 mm/yr) and HILS tide gauge minus altimetry ( $-3.63 \pm 0.26$  mm/yr) VLM is statistically  
 558 significant, and although over slightly different periods (1996.0-2019.3 and 1993.0-2018.0  
 559 respectively) suggests a bias between these techniques at the two tide gauges.

560 The difference between the two tide gauge's VLM from the InSAR and tide gauge  
 561 minus altimetry as shown on the right-hand-side ('site' 5) of Figure 5 is important. The close  
 562 proximity of these two sites (~30 km) allows the comparison of the differential VLM from  
 563 these two independent techniques, and it indicates that they produce similar results, at least  
 564 for this experiment. It suggests that while there may be offsets in one (or both) of these  
 565 techniques, the differential VLM from each is in reasonably good agreement within  
 566 uncertainty. The differential agreement between FREM and HILS for independent altimetry  
 567 minus tide gauge and TSX, and also HIL1 and CUA1 indicates that the TSX phase ramp  
 568 removes most of any long-wavelength atmospheric or orbital ramp that may have affected the  
 569 TSX rates at Fremantle. Any remaining differences are most likely a combination of the  
 570 uncertainty within the tide gauge, altimetry, cGPS and TSX measurements.

571

572 **4. Conclusion**

573 Differential VLM rates from TSX appear to deliver similar precision to that estimated from  
574 first order differential levelling in the study of Lyon et al. (2018; both around  $\pm 0.4$  mm/yr to  
575  $\pm 0.5$  mm/yr), although this is dependent on the time period and number of observations in  
576 each. Differential TSX rates give a reasonable agreement with tide gauge minus altimetry  
577 differential VLM between the two tide gauges, supporting the TSX processing methods and  
578 removal of long-wavelength systematic errors by the phase ramp. When comparisons are  
579 made for the 2012.8 – 2017.8 period among VLM rates from TSX referenced to IGS08 at  
580 PERT, altimetry minus tide gauge and cGPS rates in IGS08, there appear to be systematic  
581 offsets. It is not yet clear if this is the limit of the techniques' precision, the result of  
582 systematic differences between the techniques, or their accuracy within their respective  
583 reference frames over this shorter time period.

584 TSX VLM at FREM referenced to IGS08 at PERT cGPS is  $+0.45 \pm 0.40$  mm/yr for  
585 2012.8-2017.8. This slight uplift is different to long-term subsidence rates of  $-1.66$  mm/yr  
586 from tide gauge minus altimetry for 1993-2018, suggesting non-linear VLM at FREM.  
587 However, this should be viewed cautiously considering the possibility of a systematic bias of  
588 up to 1 mm/yr in the tide gauge minus altimetry VLM rate, and also that when approximate  
589 TRF cGPS uncertainties are propagated into the TSX rates, these (probably upper bound)  
590 uncertainties can approach  $\pm 1$  mm/yr.

591 These InSAR results suggest that when longer time series are acquired over more tide  
592 gauges, InSAR may provide remotely sensed estimates of differential VLM for tide gauge  
593 'geodetic ties' that could be extended globally. The need for geodetic ties for global tide  
594 gauges to support sea level studies is made by Woodworth et al (2017, and others), so that the  
595 continued acquisition of InSAR to build long time series over tide gauges is of high  
596 importance to facilitate more detailed tide gauge VLM analyses in the future.

597 **Acknowledgments**

598 We would like to thank the following organisations for providing and/or funding these data.  
599 TerraSAR-X scenes are acquired under the German Space Center's (DLR's) Science Project  
600 LAN1499, funded by AuScope under the Australian Geophysical Observing System  
601 (AGOS), and Australian Research Council (ARC) Linkage Projects LP 110100284 and  
602 LP140100155. The Ssalto/Duacs altimeter products were produced and distributed by the  
603 Copernicus Marine and Environment Monitoring Service (CMEMS)  
604 (<http://marine.copernicus.eu>). Dynamic atmospheric Corrections are produced by CLS using  
605 the Mog2D model from Legos and distributed by Aviso+, with support from CNES  
606 (<https://www.aviso.altimetry.fr/>). GPS data was obtained from Nevada Geodetic Laboratory  
607 at <http://geodesy.unr.edu/>. Monthly sea level means were obtained from the Permanent  
608 Service for Mean Sea Level (PSMSL) <https://psmsl.org/>. We would also like to thank  
609 Professor Andy Hooper for making StaMPS software freely available and the Delft  
610 University of Technology for providing the Doris software. Figures 1-5 were plotted using  
611 the Generic Mapping Tools (Wessel et al. 2013)

612

613 **Data availability**

614 The TerraSAR-X scenes are available to us under licence through DLR Science Project  
615 LAN1499, so cannot be made publicly available.  
616 ULR6 and NGL rates obtained from SONEL (<https://www.sonel.org/>). Processed GPS data  
617 are freely available at Nevada Geodetic Laboratory <http://geodesy.unr.edu/>, and also SONEL  
618 <https://www.sonel.org/-ULR-112-.html>.  
619 Monthly sea level records are freely available at PSMSL <https://psmsl.org/>.  
620 Altimetry data is available at CMEMS <http://marine.copernicus.eu>

621 Dynamic atmospheric corrections (DAC) are available from Aviso+ at

622 <https://www.aviso.altimetry.fr/>

623

## 624 **References**

625 Adamska LM (2012) Use of persistent scatterer interferometry for the enhancement of vertical land movement  
626 measurement at tide gauges around the British coast. PhD thesis, University of Nottingham, UK.

627 Agram PS, Simons M (2015) A noise model for InSAR time series. *Journal of Geophysical Research: Solid*  
628 *Earth*, 120(4):2752-2771, doi:10.1002/2014JB011271.

629 Altamimi Z, Collilieux X, Metivier L (2011) ITRF2008: An improved solution of the International Terrestrial  
630 Reference Frame. *Journal of Geodesy*, 85(5): 457-473, doi:10.1007/s00190-011-0444-4.

631 Bekaert DPS, Hooper A, Wright TJ (2015) A spatially variable power-law tropospheric correction technique for  
632 InSAR data. *Journal of Geophysical Research: Solid Earth*, 120(2):1345-1356, doi:10.1002/2014JB011558.

633 Bekaert DPS, Hamlington BD, Buzzanga B, Jones CE (2017) Spaceborne synthetic aperture radar survey of  
634 subsidence in Hampton Roads, Virginia (USA). *Science Reports*, 7: 14752, doi:10.1038/s41598-017-15309-  
635 5.

636 Bevis M, Scherer W, Merrifield M (2002) Technical issues and recommendations related to the installation of  
637 continuous GPS stations at tide gauges. *Marine Geodesy*, 25(1-2): 87-99,  
638 doi:10.1080/014904102753516750.

639 Blewitt G, Kreemer C, Hammond WC, Gazeaux J (2016) MIDAS robust trend estimator for accurate GPS  
640 station velocities without step detection. *Journal of Geophysical Research: Solid Earth*, 121(3): 2054-2068,  
641 doi:10.1002/2015JB012552.

642 Blewitt G, Hammond WC, Kreemer C (2018) Harnessing the GPS data explosion for interdisciplinary science,  
643 *EOS – Transactions of the American Geophysical Union*, 99, doi: 10.1029/2018EO104623.

644 Brooks BA, Merrifield MA, Foster J, Werner CL, Gomez F, Bevis M, Gill S (2007) Space geodetic  
645 determination of spatial variability in relative sea level change, Los Angeles basin. *Geophysical Research*  
646 *Letters*, 34(1), L01611, doi:10.1029/2006GL028171.

647 Burgette R, Watson CS, Church JA, Tregoning P, Coleman R (2013), Characterizing and minimizing the effects  
648 of noise in tide gauge time series: Relative and geocentric sea level rise around Australia, *Geophysical*  
649 *Journal of International*, 194(2): 719-736, doi:10.1093/gji/ggt131.

- 650 Cao·Y, Li Z, Wei·J, Hu J, Duan M, Feng G (2018) Stochastic modeling for time series InSAR: with emphasis  
 651 on atmospheric effects. *Journal of Geodesy*, 92(2):185–204, doi.org/10.1007/s00190-017-1055-5
- 652 Dheenathayalan P, Small D, Schubert A, Hanssen RF (2016) High-precision positioning of radar scatterer.  
 653 *Journal of Geodesy*, 90(5): 403-422, doi: 10.1007/s00190-015-0883-4.
- 654 Dheenathayalan P, Cuenca MC, Hoogeboom P, Hanssen RF (2017) Small reflectors for ground motion  
 655 monitoring with InSAR. *IEEE Transactions on Geoscience and Remote Sensing*, 55(12): 6703-6712, doi:  
 656 10.1109/TGRS.2017.2731424.
- 657 Fattahi H, Amelung F (2014) InSAR uncertainty due to orbital errors. *Geophysical Journal International*,  
 658 199(1), 549–560, doi: 10.1093/gji/ggu276.
- 659 Fattahi H, Amelung F (2015) InSAR bias and uncertainty due to systematic and stochastic tropospheric delay.  
 660 *Journal of Geophysical Research: Solid Earth*, 120(12):8758-8773, doi:10.1002/2015JB012419.
- 661 Featherstone WE, Penna NT, Filmer MS, Williams SDP (2015) Nonlinear subsidence at Fremantle, a long-  
 662 recording tide gauge in the Southern Hemisphere. *Journal of Geophysical Research: Oceans* 120(10): 7004-  
 663 7014, doi: 10.1002/2015JC011295.
- 664 Ferretti A, Prati C, Rocca F (2001) Permanent scatterers in SAR Interferometry. *IEEE Transactions on*  
 665 *Geoscience and Remote Sensing*, 39(1): 8-20, doi: 10.1109/36.898661
- 666 Fielding EJ, Blom RG, Goldstein RM (1998) Rapid subsidence over oil fields measured by SAR interferometry.  
 667 *Geophysical Research Letters*, 25(17): 3215-3218, doi: 10.1029/98GL52260
- 668 Garthwaite M (2017) On the design of radar corner reflectors for deformation monitoring in multi-frequency  
 669 InSAR. *Remote Sensing*, 9(7): 648, doi:10.3390/rs9070648.
- 670 Gomba G, Gonzalez FR, De Zan F (2017) Ionospheric Phase Screen Compensation for the Sentinel-1 TOPS and  
 671 ALOS-2 ScanSAR Modes. *IEEE Trans. Geosci. Remote Sens.* 55 (1), 223-235.
- 672 Hamlington BD, Thompson P, Hammond WC, Blewitt G, Ray RD (2016) Assessing the impact of vertical land  
 673 motion on twentieth century global mean sea level estimates. *Journal of Geophysical Research Oceans*,  
 674 121(7): 4980-4993, doi: 10.1002/2016JC011747.
- 675 Hammond WC, Burgette RJ, Johnson KM, Blewitt G. (2018) Uplift of the Western Transverse Ranges and  
 676 Ventura Area of Southern California: A four-technique geodetic study combining GPS, InSAR, levelling,  
 677 and tide gauges *Journal of Geophysical Research - Solid Earth*, 123(1): 836–858, doi:  
 678 10.1002/2017JB014499.
- 679 Hanssen RF (2001). *Radar Interferometry: Data Interpretation and Error Analysis*, Kluwer, Academic.

- 680 Holgate SJ, Matthews A, Woodworth PL, Rickards LJ, Tamisiea ME, Bradshaw E, Foden PR, Gordon KM,  
681 Jevrejeva S, Pugh J (2013) New data systems and products at the permanent service for mean sea level,  
682 *Journal of Coastal Research*, 29(3), 493-504, doi:10.2112/JCOASTRES-D-12-00175.1.
- 683 Hooper A (2008) A multi-temporal InSAR method incorporating both persistent scatterer and small baseline  
684 approaches. *Geophysical Research Letters*, 35(16):L16302, doi: 10.1029/2008GL034654.
- 685 Hooper A, Zebker HA (2007) Phase unwrapping in three dimensions with application to InSAR time series.  
686 *Journal of the Optical Society of America A*, 24(9): 2737-2747, doi: 10.1364/JOSAA.24.002737.
- 687 Hooper A, Bekaert D, Spaans K, Arikian M (2012), Recent advances in SAR interferometry time series analysis  
688 for measuring crustal deformation. *Tectonophysics*, 514–517: 1-13, doi:10.1016/j.tecto.2011.10.013.
- 689 Kampe, B (2006). Radar interferometry: persistent scatterer technique. Springer, Dordrecht.
- 690 Kampes B, Usai S (1999) Doris: The Delft object-oriented Radar Interferometric software. In: proceedings ITC  
691 2nd ORS symposium, August.
- 692 King MA, Keshin M, Whitehouse PL, Thomas ID, Milne M, Riva RE (2012) Regional biases in absolute sea-  
693 level estimates from tide gauge data due to residual unmodeled vertical land movement. *Geophysical*  
694 *Research Letters*, 39(14), L14604, doi:10.1029/2012GL052348.
- 695 Kuo CY, Shum CK, Braun A, Mitrovica JX, (2004) Vertical crustal motion determined by satellite altimetry and  
696 tide gauge data in Fennoscandia. *Geophysical Research Letters*, 31(1): L01608,  
697 doi:10.1029/2003GL019106.
- 698 Le Cozannet G, Raucoules D, Wöppelmann G, de Michele M, Poupardin A (2014) InSAR monitoring of ground  
699 motions impacts for in-situ sea level measurement: the example of Dakar (Senegal). IGARSS, Quebec City,  
700 QC, Canada, 13-18 July 2014, doi: 10.1109/IGARSS.2014.6946588
- 701 Le Cozannet G, Raucoules D, Wöppelmann G, Garcin M, Da Sylva S, Meyssignac B, Gravelle M, Lavigne F  
702 (2015) Vertical ground motion and historical sea-level records in Dakar (Senegal). *Environmental Research*  
703 *Letters*, 10: 084016, doi: 10.1088/1748-9326/10/8/084016.
- 704 Lyon TJ, Filmer MS, Featherstone WE (2018) On the use of repeat leveling for the determination of vertical  
705 land motion: artifacts, aliasing and extrapolation errors. *Journal of Geophysical Research: Solid Earth*,  
706 123(8):7021-7039, doi: 10.1029/2018JB015705.
- 707 Mahapatra P, Samiei-Esfahany S, van der Marel H, Hanssen R (2014) On the Use of Transponders as Coherent  
708 Radar Targets for SAR Interferometry. *IEEE Transactions on Geoscience and Remote Sensing*, 52(3): 1869,  
709 doi: 10.1109/TGRS.2013.2255881.

- 710 Mahapatra P, van der Marel H, van Leijen F, Samiei-Esfahany S, Klees R, Hanssen R (2018) InSAR datum  
 711 connection using GNSS-augmented radar transponders. *Journal of Geodesy*, 92(1):21–32,  
 712 doi:10.1007/s00190-017-1041-y.
- 713 Mazzotti S, Jones C, Thomson RE (2008) Relative and absolute sea level rise in western Canada and  
 714 northwestern United States from a combined tide gauge-GPS analysis. *Journal of Geophysical Research -*  
 715 *Oceans*, 113, C11019, doi:10.1029/2008JC004835.
- 716 Merrifield MA, Thompson PR (2018) Interdecadal sea level variations in the Pacific: Distinctions between the  
 717 tropics and extratropics. *Geophysical Research Letters*, 45(13):6604-6610, doi: 10.1029/2018GL077666
- 718 Parker AL, Filmer MS, Featherstone WE (2017) First results from Sentinel-1A InSAR over Australia:  
 719 Application to the Perth Basin. *Remote Sensing* 9(3): 299; doi: 10.3390/rs9030299.
- 720 Peltier WR (2004) Global glacial isostasy and the surface of the ice-age Earth: The ICE-5G (VM2) Model and  
 721 GRACE, *Annual Review of Earth and Planetary Sciences*, 32: 111-149, doi:  
 722 10.1146/annurev.earth.32.082503.144359.
- 723 Pfeffer J, Allemand P (2016) The key role of vertical land motions in coastal sea level variations: A global  
 724 synthesis of multisatellite altimetry, tide gauge data and GPS measurements. *Earth and Planetary Science*  
 725 *Letters*, 439: 39-47, doi: 10.1016/j.epsl.2016.01.027.
- 726 Poitevin C, Wöppelmann G, Raucoules D, Le Cozannet G, Marcos M, Testut L (2019) Vertical land motion and  
 727 relative sea level changes along the coastline of Brest (France) from combined space-borne geodetic  
 728 methods *Remote Sensing of Environment*, 222: 275-285, doi:10.1016/j.rse.2018.12.035
- 729 Raucoules D, Le Cozannet G, Wöppelmann G, de Michele M, Gravelle M, Daag A, Marcos M (2013) High  
 730 nonlinear urban ground motion in Manila (Philippines) from 1993 to 2010 observed by DInSAR:  
 731 implications for sea-level measurements. *Remote Sensing of Environment*, 139:386-397,  
 732 doi:10.1016/j.rse.2013.08.021.
- 733 Rucci A, Ferretti A, Monti Guarnieri A, Rocca F (2012) Sentinel 1 SAR interferometry applications: The  
 734 outlook for sub millimeter measurements. *Remote Sensing of Environment*, 120:156-163, doi:  
 735 10.1016/j.rse.2011.09.030.
- 736 Santamaría-Gómez A, Gravelle M, Dangendorf S, Marcos M, Spada G, Wöppelmann G (2017) Uncertainty of  
 737 the 20th century sea-level rise due to vertical land motion errors, *Earth and Planetary Science Letters*, 473:  
 738 24–32, doi: 10.1016/j.epsl.2017.05.038.
- 739 Vaniček P, Castle RO, Balaz, EI (1980) Geodetic levelling and its applications. *Reviews of Geophysics and*

- 740 *Space Physics*. 18(2), 505–524. <https://doi.org/10.1029/RG018i002p00505>.
- 741 Wessel P, Smith WHF, Scharroo R, Luis J, Wobbe F (2013) Generic Mapping Tools: Improved Version  
742 Released. *Eos, Transactions, American Geophysical Union*, 94(45):409–420,  
743 <https://doi.org/10.1002/2013EO450001>
- 744 Williams SDP (2003) The effect of coloured noise on the uncertainties of rates estimated from geodetic time  
745 series. *Journal of Geodesy* 76 (9–10), 483–494. <https://doi.org/10.1007/s00190-002-0283-4>.
- 746 Williams SDP. (2008), CATS: GPS coordinate time series analysis software, *GPS Solutions*, 12(2), 147–153,  
747 doi: 10.1007/s10291-007-0086-4.
- 748 Williams S, Bock Y, Fang P (1998) Integrated satellite interferometry: Tropospheric noise, GPS estimates and  
749 implications for interferometric synthetic aperture radar products, *Journal of Geophysical Research –Solid*  
750 *Earth*, 103(B11): 27,051–27,067, doi:10.1029/98JB02794.
- 751 Woodworth, PL (2012) A note on the nodal tide in sea level records. *Journal of Coastal Research*, 28 (2), 316–  
752 323, doi: 10.2112/JCOASTRES-D-11A-00023.1
- 753 Woodworth PL, Wöppelmann G, Marcos M, Gravelle M, Bingley RM (2017) Why we must tie satellite  
754 positioning to tide gauge data. *EOS – Transactions of the American Geophysical Union*, 98 (4): 13–15, doi:  
755 10.1029/2017EO064037.
- 756 Woodworth PL, Melet A, Marcos M, Ray RD, Wöppelmann, G., Sasaki YN, Cirano M, Hibbert A, Huthnance  
757 JM, Monserrat S, Merrifield MA (2019) Forcing factors affecting sea level changes at the coast. *Surveys in*  
758 *Geophysics*, doi: 10.1007/s10712-019-09531-1.
- 759 Wöppelmann G, Martin Miguez B, Bouin MN, Altamimi Z (2007) Geocentric sea-level trend estimates from  
760 GPS analyses at relevant tide gauges world-wide, *Global and Planetary Change*, 57(3–4), 396–406,  
761 doi:10.1016/j.gloplacha.2007.02.002
- 762 Wöppelmann G, Le Cozannet G, De Michele M, Raucoules D, Cazenave A, Garcin M, Hanson S, Marcos M,  
763 Santamaría-Gómez, A (2013) Is land subsidence increasing the exposure to sea level rise in Alexandria,  
764 Egypt? *Geophysical Research Letters*, 40 (12): 2953–2957, doi: 10.1002/grl.50568.
- 765 Wöppelmann G, Marcos M (2016) Vertical land motion as a key to understanding sea level change and  
766 variability. *Reviews of Geophysics*, 54 (1): 64–92, doi: 10.1002/2015RG000502.
- 767